

Hitting the wall: Human sperm velocity recovery under ultra-confined conditions

SCI F

Cite as: Biomicrofluidics 14, 024108 (2020); doi: 10.1063/1.5143194

Submitted: 20 December 2019 · Accepted: 8 March 2020 ·

Published Online: 30 March 2020



View Online



Export Citation



CrossMark

Matías A. Bettera Marcat,^{1,2} María N. Callea,^{3,4} Gastón L. Miño,^{5,6} Marisa A. Cubilla,^{3,4} Adolfo J. Banchio,^{1,2} Laura C. Giojalas,^{3,4} Verónica I. Marconi,^{1,2} and Héctor A. Guidobaldi^{3,4,a)}

AFFILIATIONS

¹ Facultad de Matemática, Astronomía, Física y Computación, Universidad Nacional de Córdoba, Av. Medina Allende s/n, CP X5000HUA Córdoba, Argentina

² Instituto de Física Enrique Gaviola, UNC, CONICET, FAMAF, Av. Medina Allende s/n, CP X5000HUA Córdoba, Argentina

³ Facultad de Ciencias Exactas, Físicas y Naturales, Centro de Biología Celular y Molecular, Universidad Nacional de Córdoba, Av. Vélez Sarsfield 1611, CP X5016GCA Córdoba, Argentina

⁴ Instituto de Investigaciones Biológicas y Tecnológicas, UNC, CONICET, FCEFyN, Av. Vélez Sarsfield 1611, CP X5016GCA Córdoba, Argentina

⁵ Laboratorio de Microscopía Aplicada a Estudios Moleculares y Celulares (LAMAE), Facultad de Ingeniería, Universidad Nacional de Entre Ríos, CP 3100 Oro Verde, Argentina

⁶ Instituto de Investigación y Desarrollo en Bioingeniería y Bioinformática (IBB—UNER-CONICET), CP 3100 Oro Verde, Argentina

^{a)} Author to whom correspondence should be addressed: hector.guidobaldi@unc.edu.ar. Telephone: +54 351 535-3800 ext. 30307

ABSTRACT

Infertility is a common medical condition encountered by health systems throughout the world. Despite the development of complex *in vitro* fertilization techniques, only one-third of these procedures are successful. New lab-on-a-chip systems that focus on spermatozoa selection require a better understanding of sperm behavior under ultra-confined conditions in order to improve outcomes. Experimental studies combined with models and simulations allow the evaluation of the efficiency of different lab-on-a-chip devices during the design process. In this work, we provide experimental evidence of the dynamics of sperm interacting with a lateral wall in a shallow chamber. We observe a decrease in average sperm velocity during initial wall interaction and partial recovery after the alignment of the trajectory of the cell. To describe this phenomenon, we propose a simple model for the sperm alignment process with a single free parameter. By incorporating experimental motility characterization into the model, we achieve an accurate description of the average velocity behavior of the sperm population close to walls. These results will contribute to the design of more efficient lab-on-a-chip devices for the treatment of human infertility.

Published under license by AIP Publishing. <https://doi.org/10.1063/1.5143194>

I. INTRODUCTION

In 2015, it was estimated that approximately 186×10^6 people worldwide suffer from infertility.¹ It has been over 40 years since the first baby was conceived via *in vitro* fertilization.² However, despite efforts to improve *in vitro* fertilization techniques, it is only successful 30%–35% of the time.³ Attempts to improve the outcome performance of these techniques have been focused on enhancing the quality of gametes, particularly sperm,^{4,5} and developing more efficient miniature *in vitro* fertilization systems.^{6–10} In this miniaturization process, microfluidics has been a key tool in

the development of high-throughput sperm analysis and selection devices.^{10–14} This miniaturization process and the development of new systems on a cellular scale (i.e., lab-on-a-chip type systems) require a greater understanding of the behavior of sperm in ultra-confined conditions.

In the presence of a solid surface, interactions are essential for both artificial¹⁵ and biological microswimmers.¹⁶ In particular, spermatozoa tend to swim close to the walls.^{17–21} This cell–surface interaction could be a consequence of hydrodynamic interactions^{16,22,23} or due to steric interactions.^{24–26} When spermatozoa

swim within ultra-confined $\sim 20\text{ }\mu\text{m}$ deep chambers, they are, due to its geometry, close to the surface at all times. Sperm cells are $\sim 60\text{ }\mu\text{m}$ long, and its flagellum typically produces a helicoidal 3D movement within a cone-shaped envelope ($15\text{--}30\text{ }\mu\text{m}$ wide).^{27–29} Due to the proximity of top and bottom surfaces, cells move both in clock-wise and in counter clock-wise circular trajectories while also alternating with linear like ones.³⁰ However, the orientation of the sperm cells can be manipulated by the presence of a lateral wall, arranged as an asymmetric obstacle,¹⁸ or by designing specific geometries in the boundaries of the chamber.^{20,30} These wall interactions affect both the direction of movement and the speed of sperm cells. It has been reported that sperm velocity is reduced when the sperm is in contact with a lateral wall and is then restored to previous values when the sperm breaks free from it.³⁰ In the present work, we study the interaction between the swimming cell and a lateral wall in an ultra-confined environment where the cell interacts with three surfaces. The design and development of effective lab-on-a-chip devices based on trial-error experiments are expensive and time-consuming. Therefore, understanding the details of the sperm-wall interaction is necessary and critically important for the development of accurate models, which can be used to evaluate the theoretical efficiency during the design stage of novel lab-on-a-chip devices. Here, by means of an experimental approach, we characterize the sperm velocity transition behavior during the interaction with the lateral walls under ultra-confined conditions and test how this knowledge improves numerical predictions.

II. MATERIALS AND METHODS

A. Sperm preparation

The experiments were performed with human semen samples from normozoospermic donors who gave written consent and approved by Ethics Committee of the Hospital Nacional de Clínicas (Universidad Nacional de Córdoba, Argentina; No. 06/10/E) and treated in accordance with the Declaration of Helsinki. The spermatozoa were separated from the seminal plasma by migration sedimentation technique,³¹ and the motile sperm population was

adjusted to 5×10^6 cells/ml with the Biggers–Whitten–Whittingham culture medium (BWW),³² supplemented with 1% bovine serum albumin, and kept in an incubator at 37°C with 5% CO_2 in the air until use within 3 h.

B. Ultra-confinement chamber

Experiments were performed in a rectangular cross section chamber of $23\text{ }\mu\text{m}$ high and $450\text{ }\mu\text{m}$ width. The shape of the device was achieved with conventional soft lithography methods.³³ Molded Polydimethylsiloxane (PDMS) was glued to a glass slide using plasma bonding.³⁴ PDMS walls ensure oxygen diffusion, optical transparency, and biocompatibility with the biological sample.

C. Three-dimensional reconstruction of the cells into the device

A sperm solution was loaded into the chamber and let it dry over 24–48 h. Then, the mounting glass was carefully removed recovering the PDMS structure of the chamber with the cells (see Fig. 1). Then, it was observed and scanned with a confocal microscope OLS4100 (Olympus, Japan), and the three-dimensional structure reconstruction was performed with the Olympus LEXT software ver. 3.1.1 (Olympus, Japan).

D. Sperm-wall interaction experiments

The chamber was loaded with BWW and placed for 15 min in a vacuum chamber to extract air bubbles. Then, we loaded the sperm suspension at a final concentration of 1×10^6 cells/ml. Two minutes later, in the absence of fluid flow, we start recording the sperm movement in the ultra-confinement chamber by means of phase-contrast video-microscopy using a digital camera (Nikon, USA) connected to an inverted microscope (Nikon, USA). The recording of the tracks was performed at 10 Hz with an image resolution of 640×480 pixels with the BR Nis Elements software (Nikon, USA) using a $10\times$ objective. The image analysis was performed with the software Fiji³⁵ using the MtrackJ plug-in³⁶ to determine the sperm head trajectories of those cells interacting with

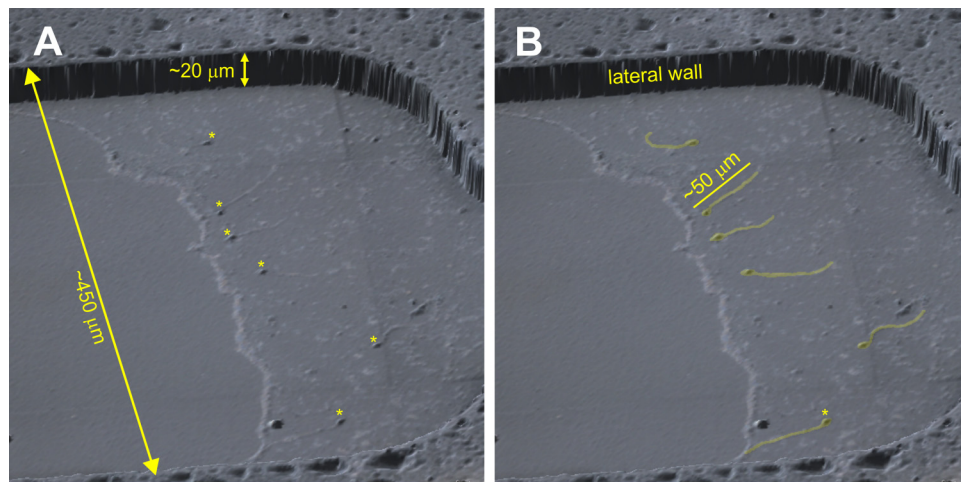


FIG. 1. Three-dimensional confocal image of the ultra-confinement chamber loaded with sperm cells. (a) Confocal 3D image showing the chamber dimensions and the location of the spermatozoa heads (*). (b) The sperm head and flagellum were artificially colored in order to facilitate the visualization of its dimensions.

planar lateral walls. Then, the kinetic parameters of the cells were calculated with a homemade macro paNoel (v1.0, Universidad Nacional de Córdoba; <http://www.iibyt.conicet.unc.edu.ar/software/>).

E. Probability density function (PDF) of sperm measurement

To determine the sperm density between the edges of the chamber, we selected a rectangular region ($450\text{ }\mu\text{m}$ width and $100\text{ }\mu\text{m}$ height) of interest over the image, matching the edges of the chamber and divided it into 45 columns ($10\text{ }\mu\text{m}$ width and $100\text{ }\mu\text{m}$ height each). We determined the sperm density by counting the number of spermatozoa in each column and dividing it by the column area ($10 \times 100\text{ }\mu\text{m}^2$). This analysis was made on phase-contrast microscopy videos.

F. Simulations

Sperm cells swim in an ultra-confined chamber that has only $\sim 20\text{ }\mu\text{m}$ of depth, producing a quasi-two-dimensional environment. Due to this confinement, we model sperm dynamics with a 2D phenomenological model. Each cell is represented by a disk, and the head motion is modeled by an oscillation around a linear trajectory, mimicking the way they swim. Sperm swimming at a low Reynolds number regime is described by a force-free and torque-free equation of motion. The Langevin equations used include a stochastic noise that represents the rotational diffusion in the direction of swimming. This model has proven satisfactory to characterize the rectification of sperm cells in microfluidics chambers.¹⁸ Now we have included an orientational interaction with walls that considers the alignment of the cell to the wall.

The i th micro-swimmer coordinates are its position, $\vec{x}_i(t)$, and the orientation of its mean translational velocity, $\varphi_i(t)$. The dynamical equations for a system of N micro-swimmers are as

follows:

$$\gamma d\vec{x}_i(t)/dt = \vec{F}_i^m + \vec{F}_i^{ss}(\vec{x}_i(t)) + \vec{F}_i^{sw}(\vec{x}_i(t)), \quad (1)$$

where γ is the translational drag coefficient, \vec{F}_i^m is the motor force that represents the micro-swimmer propulsion, $\vec{F}_i^{ss}(\vec{x}_i(t))$ is the interaction force between micro-swimmers, and $\vec{F}_i^{sw}(\vec{x}_i(t))$ is the interaction force between the micro-swimmer and the wall.¹⁸

The motor force has two terms, one responsible for the mean translational velocity and the other for the head oscillation,

$$\vec{F}_i^m = \gamma[v_i^m \hat{e}_i^{\parallel}(\varphi_i) + 2\pi f A_h \cos(2\pi f t + \phi_i) \hat{e}_i^{\perp}(\varphi_i)], \quad (2)$$

where v_i^m is the mean translational velocity of the i th micro-swimmer, A_h and f are the heading amplitude and frequency, ϕ_i is the phase shift of the i th micro-swimmer heading, and $\hat{e}_i^{\parallel}(\varphi_i)$ and $\hat{e}_i^{\perp}(\varphi_i)$ are the unit vectors parallel and orthogonal to the translation direction, respectively.

The evolution of the angular coordinate $\varphi_i(t)$ at each time step, Δt , is given by

$$\varphi_i(t + \Delta t) = \varphi_i(t) + \left[-\Delta t \sum_k \zeta \beta_{ik}(\varphi_i(t)) \Theta\left(1 - \frac{r_{i,k}}{r_s + h}\right) \right] / \gamma_r + v \sqrt{2 D_r \Delta t}. \quad (3)$$

In Eq. (3), γ_r is the rotational drag coefficient and ζ is the alignment parameter that has units $[\zeta] = [\gamma_r]/\text{s}$, where s means seconds. In the following, we will refer to the adimensional parameter $\xi = \zeta/s \cdot \gamma_r$. Meanwhile, $\beta_{ik}(\varphi_i(t))$ is the angle between the mean velocity direction of the i th micro-swimmer and the k th wall, $r_{i,k}$ is the distance from the i th micro-swimmer to the k th wall, r_s is the radius of the disk, and h is the threshold distance to the wall at

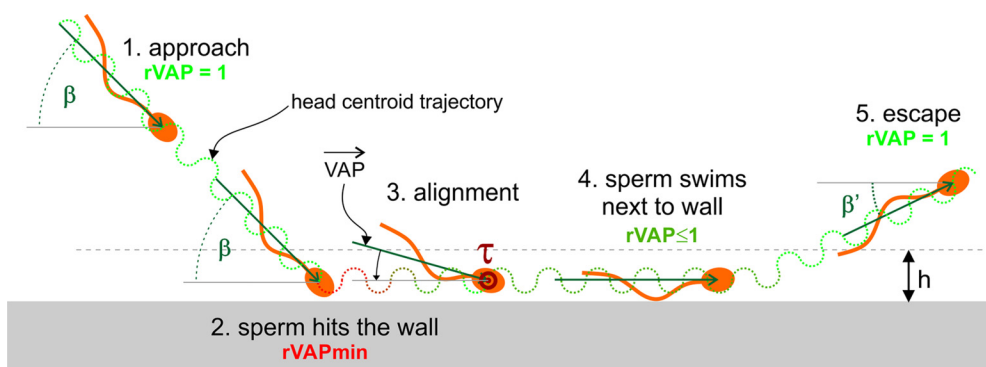


FIG. 2. Sketch of the working model for sperm interaction with the lateral wall. In simulations, we model the interaction process with a phenomenological alignment, depending linearly on the incidence angle. (1) Sperm approaches with a mean relative average velocity (rVAP) of 1. (2) When the sperm hits the wall, depending on the angle of incidence (β) of $\overline{\text{VAP}}$, the rVAP drops to a minimum value (rVAPmin). (3) A phenomenological alignment (τ) acting on the cell when it is closer than a distance h to the wall, reorient $\overline{\text{VAP}}$ parallel to the surface. (4) Then, the sperm swims with a mean $\text{rVAP} \leq 1$ next to the wall until it escapes (5) due to the rotational diffusion effect.

which point the alignment begins to influence the micro-swimmers since the hydrodynamic interactions decay after few bodies of distance from a surface;²² v is a stochastic Gaussian noise and D_r is the rotational diffusion coefficient. The only free parameter is ξ , and it is included to fit the time scale of the sperm velocity recovery in the wall proximity.

1. Average path velocity (VAP) and probability density function (PDF) definitions

One of the experimentally measured quantities during the sperm Approaching-Aligning-Swimming-Escape event (AASE event) as illustrated in Fig. 2 is average path velocity (VAP),³⁷ which captures the mean velocity of the sperm averaged typically (in experiments) for several heading periods. In simulations, given that the phase of the heading process is known at each time step, we calculate the VAP simply by sampling positions separated by one period of the heading, T , namely,

$$\text{VAP}_i(t) = \|\vec{x}_i(T+t) - \vec{x}_i(t)\|/T, \quad (4)$$

where period $T = 1/f$. In simulated trajectories, with this definition, the effects of the heading are suppressed and the VAP is consistent with the definition used for experimental data analysis.³⁷

The PDF as a function of the distance to a wall has been studied for sperm cells as well as for bacteria.^{17,18,23} It allows quantifying the cell/bacteria accumulation close to walls, which is a consequence of the dynamics of the microswimmers. We compute the PDF in a similar way as in the experiments, i.e., dividing the distance between walls by the same number of bins to count the sperm cells. In this way, the results may be fairly compared.

G. Simulation parameters

The input parameters for the simulations are not adjustable but taken from experimental data analysis. They are mean translational velocity $v^m = 28\text{ }\mu\text{m/s}$, heading amplitude $A_h = 1.5\text{ }\mu\text{m}$, beat cross frequency $f = 10\text{ Hz}$, the disk radius $r_s = 2.5\text{ }\mu\text{m}$, time step $\Delta t = 0.001\text{ s}$, alignment threshold distance $h = 5\text{ }\mu\text{m}$ (one disk diameter), and rotational diffusion coefficient $D_r = 0.01\text{ rad}^2/\text{s}$. For more details of the swimmer-wall and swimmer-swimmer interactions, see Ref. 18.

To compute the VAP during the AASE event, 16 simulations with 4000 cells each were performed. The cells at the initial time, t_i , were positioned at a distance d of the wall (chosen for most of the cells arriving to it in 2 s) and had an incidence angle, β_i (defined as the angle between the lateral wall and the i -sperm velocity direction), that was set to one of the 16 values $\{15^\circ, 20^\circ, 25^\circ, \dots, 85^\circ, 90^\circ\}$. In this way, a set of 64 000 AASE events were generated for each ξ value, which afterward was grouped according to the actual incidence angle at the instant the cell contacts the wall (this time was set to $t=0$ for each trajectory/event). The ranges that determined the groups were $[15^\circ, 20^\circ]$, $(20^\circ, 25^\circ]$, ..., $(85^\circ, 90^\circ]$. Note that due to rotational diffusion the incidence angle may differ from the corresponding initial value β_i . Finally, we averaged all the time-dependent VAPs within each incidence angle group. The region simulated is a large rectangular box with dimensions

$450 \times 3000\text{ }\mu\text{m}^2$ with parallel walls at the right and left edges. We cover the ξ range $[10^{-2}, 10^2]$. To study the cell density distribution, we have used a different simulation setup in which the interactions with other swimmers are relevant. The region simulated is a large rectangular box with dimensions $450 \times 4500\text{ }\mu\text{m}^2$ with parallel walls at the right and left edges and periodic boundary conditions in the y -direction. We use the same experimental density $\rho = 2.604 \times 10^{-4}\text{ cells}/\mu\text{m}^2$ (from video-microscopy) with $N = 527$ cells in simulations.

III. RESULTS AND DISCUSSIONS

We evaluate sperm behavior during the interaction with lateral walls under ultra-confined conditions. To better understand and visualize the ultra-confinement conditions, we made a three-dimensional reconstruction of the chamber loaded with sperm. Figures 1(a) and 1(b) show the human sperm size in relation to the chamber dimensions. The spermatozoa have a filamentous shape, with an oval head of $\sim 6 \times 4\text{ }\mu\text{m}$ and a thickness of $\sim 1.5\text{ }\mu\text{m}$. In Fig. 1(b), it has been remarked the head, the midpiece, and the principal piece of the flagellum, with a length of $\sim 50\text{ }\mu\text{m}$. The end piece cannot be observed at optical microscope resolution, but its length is $\sim 10\text{ }\mu\text{m}$. When swimming, the filamentous flagellum acquires a three-dimensional “cone” shape,²⁷ which in turn hits the surfaces of the chamber confining the sperm movement. Then, to characterize the translational movement of the sperm, we follow the trajectories under phase-contrast video-microscopy [Fig. 3(a) (Multimedia view)]. In this condition, the borders of the ultra-confinement chamber showed a refraction that reduced the contrast of the sperm cells swimming next to the borders [Fig. 3(a) (Multimedia view)]. Hence, to properly determine the trajectories, we follow the sperm heads manually. Despite that, this method is time-consuming; under these conditions, it is more reliable than automatic tracking that easily loses the sperm next to walls. By means of the (x,y) coordinates, we determined the average sperm velocity (VAP) for each point along the trajectory and represented the VAP with a color dot located in the (x,y) coordinates with a homemade Fiji macro [Fig. 3(b)]. This method allows to visually analyze the sperm behavior, and as observed in Fig. 2, sperm swimming far from the wall moves with a determined VAP that seems to suddenly drop when it reaches the wall, and after a period of being swimming next to it, the sperm velocity seems to be recovered. To better characterize the sperm behavior, we followed 56 cells with trajectories of at least 2 s prior to reach the wall, and another 3 s at least, swimming next to the wall. Since the sperm showed a wide range of VAP intra- and inter-trajectories, we determined the relative value of VAP (rVAP) considering as 100% the mean velocity prior to the arrival at the wall [$t=0\text{ s}$; Fig. 3(c)]. As observed in Fig. 3(c), when the sperm reaches the wall, the rVAP of sperm decreases and then is partially recovered (around 80%) during the first 2 s after hitting the wall [Fig. 3(d)]. We observed a wide variety of minimum rVAP ($rVAP_{\min}$) among the cells [Fig. 3(c)]. This variation could be a consequence of the incidence angle, i.e., the angle before approaching the surface. To test this hypothesis, we determined the incidence angle (β) between the trajectory and the plane of the lateral wall and then we evaluate the correlation between β and $rVAP_{\min}$. As observed

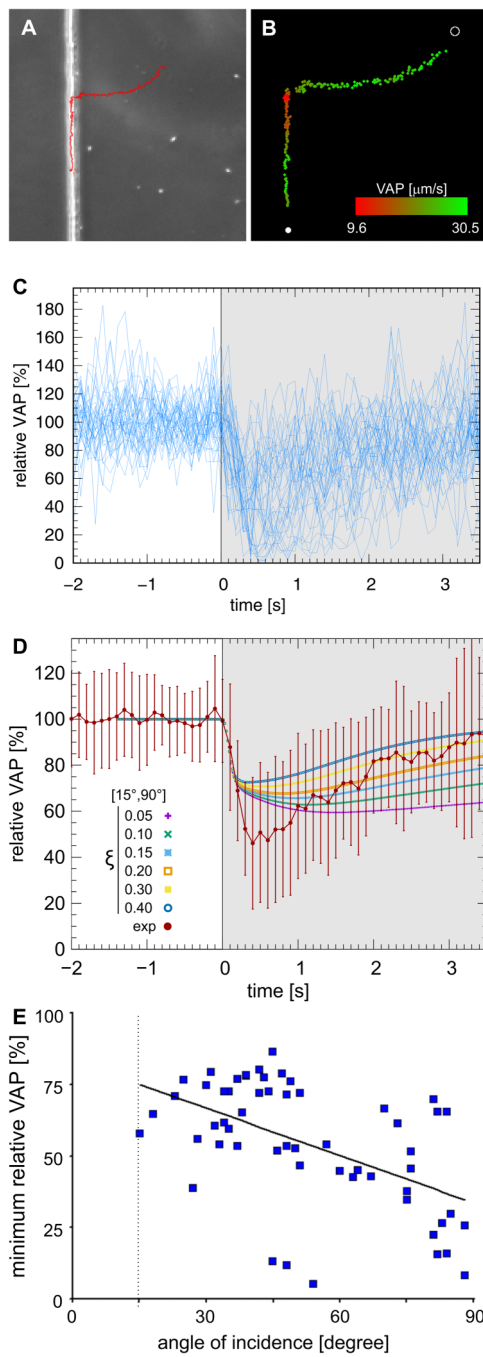


FIG. 3. Characterization of a sperm AASE event against the lateral wall under ultra-refinement (depth $\sim 20 \mu\text{m}$). Sperm trajectory (a) and the velocity of the average path (VAP) along the trajectory of a representative cell (b). Representation of the relative VAP (rVAP) of 56 sperm trajectories aligned at the moment of the arrival to the wall (time = 0 s); and (c) the mean value of rVAP \pm SD (d) showing diminution and partial recovery of rVAP during the AASE event. Correlation between the angle of incidence and the minimum rVAP registered for each trajectory (e). Multimedia view: <https://doi.org/10.1063/1.5143194.1>

in Fig. 3(e), there is an inverted correlation between both quantities ($r = -0.53; P < 0.0001$). When the cell swims perpendicular to the lateral wall, lower is the $rVAP_{\min}$. The data dispersion observed could be a consequence of minor defects or rugosity at the walls [Fig. 1(a)] or the precision in determining the incidence angle during the AASE event due to video resolution [Fig. 3(a)]

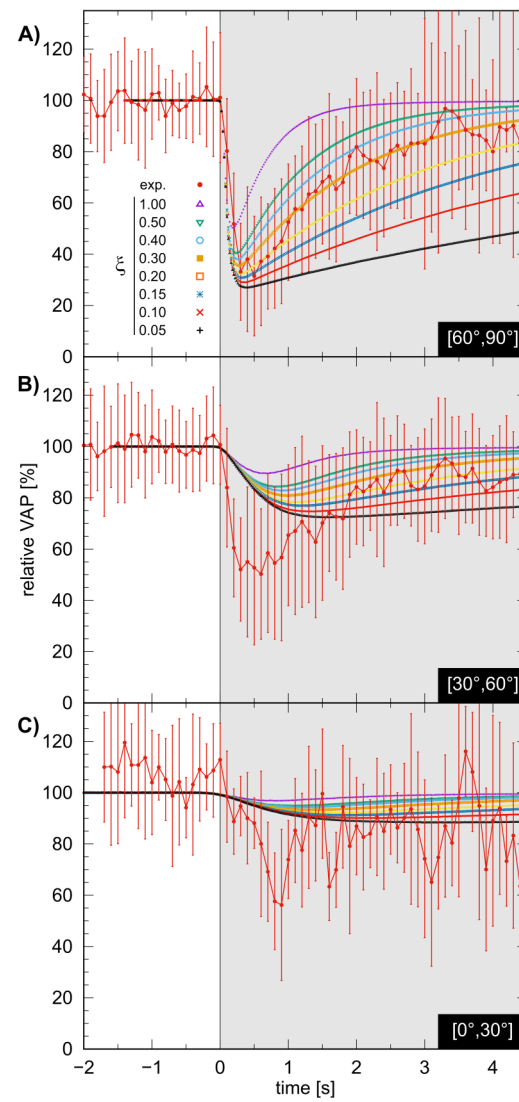


FIG. 4. Experiments and simulations of rVAP of the sperm in an AASE event with a straight wall. The sperms were grouped according to the angle of incidence (β_i) in three groups: (a) $60^\circ < \beta_i < 90^\circ$ ($N = 23$), (b) $30^\circ < \beta_i < 60^\circ$ ($N = 22$), and (c) $0^\circ < \beta_i < 30^\circ$ ($N = 7$). In parallel, a simulation was performed with the same number of sperm and the same distribution of angles of incidence. The simulations reproduce with fine accordance the qualitative behavior of velocity temporal evolution of sperms colliding a wall. The adequate values of the ξ parameter are 0.2–0.4 for its closeness with the mean velocity. The rVAP in the simulations was calculated for a range of ξ parameter between 0.05 and 1.

(Multimedia view)]. However, $rVAP_{min}$ seems to be stable for $\beta < 60^\circ$, but the deceleration seems more pronounced for higher angles of incidence.

In order to further understand the behavior of the sperm during the AASE event, we evaluate the correlation between β_i and the calculated $rVAP_{min}$. We group the cells according to the following β_i ranges: $[0^\circ, 30^\circ]$, $[30^\circ, 60^\circ]$, and $[60^\circ, 90^\circ]$. As observed in Fig. 4, for higher angles of incidence [Fig. 4(a)], there is a pronounced decrease of $rVAP_{min}$ (red dots), which is less evident at lower β_i [Figs. 4(b) and 4(c)]. However, regardless of the drop in $rVAP$, the cells seem to restore roughly an 80% of the $rVAP$ (before touching the wall), within the first 2 s while swimming next to the wall. The behavior of the cell during the AASE event suggests that the sperm first arrives at the wall and then, due to the beat of the flagellum and the hydrodynamic interactions produced by the wall, reorients the flagellum-head axis and continues the displacement following the boundary and recovering the $rVAP$ (Fig. 2). To test this hypothesis, we simulate the sperm movement near the environment of lateral walls. Simulations show that, after reaching a wall, the sperm experiences a reduction of $rVAP$ due to its oblique alignment with the wall. The incident direction has a component that is compensated by the normal force of the wall, and as the cell aligns parallel, due to the phenomenological alignment, recovers its velocity (Fig. 2). We can tune the alignment parameter, ξ , in order to reproduce the time scale from the experimentally observed alignment process. In Fig. 4, the simulated velocity evolutions are plotted for a range of ξ values and different incidence angles, and in each case, they are compared with the experimental values. To obtain ξ values that properly reproduce human sperm dynamics, we studied the Mean Squared Error (MSE), the deviation of simulations from the experimental $rVAP$ and from the Probability Density Function (PDF) (see the supplementary material). In the analysis of $rVAP$'s MSE, we find a minimum at $\xi = 0.225$, while from the PDF, the minimum occurs at $\xi = 0.12$. Therefore, we suggest that the range of ξ values that reproduce dynamics are in the interval $[0.1, 0.25]$, and we propose as the optimum value $\xi_{op} \approx 0.17$.

Then, we test whether the incorporation of the sperm velocity transition when hitting the wall would improve the sperm behavior simulations. Therefore, we determined experimentally the probability of sperm density distribution in the ultra-confinement chamber, and we compare with simulations with and without orientational interaction with lateral walls. As observed in Fig. 5, the sperm probability density function is higher next to the wall, due to the wall interaction, while it remains homogeneous in the middle of the chamber. Sperm probability distribution obtained by simulation is in qualitative agreement with the experimental results. Moreover, the inclusion of sperm velocity transitions during the wall collision ($\xi \neq 0$) improves the simulation outcome with a much better correlation between the experiment and the simulation data with relative errors $< 2\%$ (see Fig. 5 and Fig. S3 in the supplementary material).

Under ultra-confined conditions, surface interfaces influence the way in which mammalian spermatozoa swim. Sperm generally swim adjacent to the lateral wall as a consequence of hydrodynamic interactions.²² Additionally, due to their conical shape resulting from the beating movement of the flagellum,³⁸ the sperm trajectory

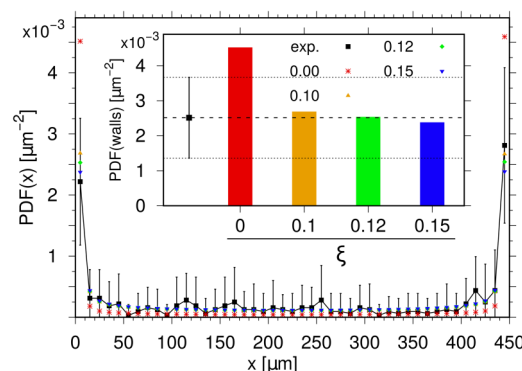


FIG. 5. Experimental and simulated probability density function (PDF) of the spermatozoa in the ultra-confinement chamber. The incorporation of $\xi \neq 0$ in the simulation model of the sperm movement improves the prediction of the behavior of the cells under ultra-confinement conditions (relative errors $< 2\%$). Inset: Experimental PDF at the wall, predicted PDF without ($\xi = 0$) and with ($0.1 < \xi < 0.2$), and the simulation of the sperm velocity transition during wall collision.

follows the shape of the lateral boundaries.^{18,30} In this context, it has been reported that the velocity of the sperm swimming alongside the walls is reduced.^{30,39} Here, we provide experimental evidence of the dynamics of the sperm during the transition from a two-wall (upper and bottom) to three-wall confinement. In a shallow chamber ($\sim 20 \mu\text{m}$ deep), when a sperm encounters a lateral wall, the translational velocity is suddenly reduced and, in some cases, the cell completely stops. This observation is consistent with the idea that the sperm collides the wall when it reaches it. This is also supported by the fact that there is a correlation between the angle of incidence and sperm velocity reduction, where small incidence angles present a low reduction in the average sperm speed. Besides, we did not observe an angle of incidence below 15° which may reflect the limit imposed by the shape of the cone formed by the flagellar beating and the length of the sperm.³⁸ After collision with the wall, the sperms partially restore their average velocity. In *Escherichia coli*, it has been observed that the reduction of velocity is relevant when there are a few bodies of distance between the bacterium and the wall, as well as the alignment that occurs when the bacteria is in contact (distances lower than its long dimension) with the wall.²⁶ Sperm cells seem to follow a similar pattern since the alignment and the restoration of the translational movement occur in close proximity to the wall [Fig. 1(b)]. Hence, using a simple model that better describes the wall interaction, we were able to simulate sperm behavior and compare the numerical results with experimental data obtaining good concurrence. These promising results will contribute to the development of more efficient lab-on-a-chips, where the micro- and ultra-confinement conditions modify sperm population transport and dynamic properties (e.g., sperm concentration, sorting, selection, cell re-concentration times, etc.). An accurate model is required in order to design and fabricate lab-on-a-chips with different shapes and dimensions, thereby avoiding wide ranges of experimental trials and reducing time and costs in the development process.

IV. CONCLUSIONS

Using real motility parameters and with only a simple model for the alignment process with a single free parameter, we qualitatively reproduced the population average velocity behavior and fitted the alignment parameter of the model. Proving the correspondence of simulations and confined sperm population dynamics enables the model to produce more accurate predictions of the population average magnitudes. Hence, accurate models and simulations based on well characterized experimental data assist in developing more efficient lab-on-a-chip devices for human reproduction use in the near future.

SUPPLEMENTARY MATERIAL

See the [supplementary material](#) for a detailed explanation of the criteria used to choose the free alignment parameter, comparing simulations and experiments.

ACKNOWLEDGMENTS

This work was supported by SECyT (Universidad Nacional de Córdoba); Universidad Nacional de Entre Ríos under Grant No. PID-SCYT-UNER 6173-2017; CONICET; and Agencia Nacional de Promoción Científica y Tecnológica under Grant Nos. D-TEC 003/13, PICT 2015-0735, and PICT 2016-4116.

REFERENCES

- ¹M. C. Inhorn and P. Patrizio, *Hum. Reprod. Update* **21**, 411 (2015).
- ²P. C. Steptoe and R. G. Edwards, *Lancet* **2**, 366 (1978).
- ³S. Dyer, G. M. Chambers, J. de Mouzon, K. G. Nygren, F. Zegers-Hochschild, R. Mansour, O. Ishihara, M. Banker, and G. D. Adamson, *Hum. Reprod.* **31**, 1588 (2016).
- ⁴R. Henkel, *Asian J. Androl.* **14**, 260 (2012).
- ⁵L. V. Gatica, H. A. Guidobaldi, M. M. Montesinos, M. E. Teves, A. I. Moreno, D. R. Uñates, R. I. Molina, and L. C. Giojalas, *Mol. Hum. Reprod.* **19**, 559 (2013).
- ⁶R. S. Suh, X. Zhu, N. Phadke, D. A. Ohl, S. Takayama, and G. D. Smith, *Hum. Reprod.* **21**, 477 (2006).
- ⁷D. Lai, G. D. Smith, and S. Takayama, *J. Biophotonics* **5**, 650 (2012).
- ⁸V. F. S. Tsai, H. C. Chang, J. T. Hsieh, and A. M. Wo, *Urol. Sci.* **27**, 56 (2016).
- ⁹M. A. M. M. Ferraz, H. S. Rho, D. Hemerich, H. H. W. Henning, H. T. A. van Tol, M. Höller, U. Besenfelder, M. Mokry, P. L. A. M. Vos, T. A. E. Stout, S. Le Gac, and B. M. Gadella, *Nat. Commun.* **9**, 4934 (2018).
- ¹⁰R. Nosrati, P. J. Graham, B. Zhang, J. Riordon, A. Lagunov, T. G. Hannam, C. Escobedo, K. Jarvi, and D. Sinton, *Nat. Rev. Urol.* **14**, 707 (2017).
- ¹¹T. Chinnasamy, J. L. Kingsley, F. Inci, P. J. Turek, M. P. Rosen, B. Behr, E. Tüzel, and U. Demirci, *Adv. Sci.* **5**, 1700531 (2018).
- ¹²M. Zaferani, S. H. Cheong, and A. Abbaspourrad, *Proc. Natl. Acad. Sci. U.S.A.* **115**, 8272 (2018).
- ¹³G. Marzano, M. S. Chiriacò, E. Primiceri, M. E. Dell'Aquila, J. Ramalho-Santos, V. Zara, A. Ferramosca, and G. Maruccio, "Sperm selection in assisted reproduction: A review of established methods and cutting-edge possibilities," *Biotechnol. Adv.* (published online, 2019).
- ¹⁴C. K. Tung, L. Hu, A. G. Fiore, F. Ardon, D. G. Hickman, R. O. Gilbert, S. S. Suarez, and M. Wu, *Proc. Natl. Acad. Sci. U.S.A.* **112**, 5431 (2015).
- ¹⁵P. Bayati, M. N. Popescu, W. E. Uspal, S. Dietrich, and A. Najafi, *Soft Matter* **15**, 5644 (2019).
- ¹⁶E. Lauga, *Annu. Rev. Fluid Mech.* **48**, 105 (2016).
- ¹⁷Rothschild, *Nature* **198**, 1221 (1963).
- ¹⁸A. Guidobaldi, Y. Jeyaram, I. Berdakin, V. V. Moshchalkov, C. A. Condat, V. I. Marconi, L. Giojalas, and A. V. Silhanek, *Phys. Rev. E Stat. Nonlin. Soft Matter Phys.* **89**, 032720 (2014).
- ¹⁹J. S. Guasto, R. Rusconi, and R. Stocker, *Annu. Rev. Fluid Mech.* **44**, 373 (2012).
- ²⁰P. Denissenko, V. Kantsler, D. J. Smith, and J. Kirkman-Brown, *Proc. Natl. Acad. Sci. U.S.A.* **109**, 8007 (2012).
- ²¹R. Nosrati, A. Driouchi, C. M. Yip, and D. Sinton, *Nat. Commun.* **6**, 8703 (2015).
- ²²E. Lauga, W. R. DiLuzio, G. M. Whitesides, and H. A. Stone, *Biophys. J.* **90**, 400 (2006).
- ²³A. P. Berke, L. Turner, H. C. Berg, and E. Lauga, *Phys. Rev. Lett.* **101**, 038102 (2008).
- ²⁴G. Li and J. X. Tang, *Phys. Rev. Lett.* **103**, 078101 (2009).
- ²⁵G. Li, J. Bensson, L. Nisimova, D. Munger, P. Mahautmr, J. X. Tang, M. R. Maxey, and Y. V. Brun, *Phys. Rev. E Stat. Nonlin. Soft Matter Phys.* **84**, 041932 (2011).
- ²⁶S. Bianchi, F. Saglimbeni, and R. Di Leonardo, *Phys. Rev. X* **7**, 011010 (2017).
- ²⁷F. Silva-Villalobos, J. A. Pimentel, A. Darszon, and G. Corkidi, in *Annual International Conference of the IEEE Engineering in Medicine and Biology Society* (IEEE, 2014), p. 190.
- ²⁸M. Muschol, C. Wenders, and G. Wennemuth, *PLoS One* **13**, e0203912 (2018).
- ²⁹S. T. Mortimer, D. Schoëvaërt, M. A. Swan, and D. Mortimer, *Hum. Reprod.* **12**, 1006 (1997).
- ³⁰H. A. Guidobaldi, Y. Jeyaram, C. A. Condat, M. Oviedo, I. Berdakin, V. V. Moshchalkov, L. C. Giojalas, A. V. Silhanek, and V. I. Marconi, *Biomicrofluidics* **9**, 024122 (2015).
- ³¹N. T. Tea, M. Jondet, and R. Scholler, *In Vitro Fertilization, Embryo Transfer and Early Pregnancy* (Springer Netherlands, Dordrecht, 1984), pp. 117–120.
- ³²J. D. Biggers, W. K. Whitten, and D. G. Whittingham, *Methods in Mammalian Embryology* (W. H. Freeman & Co., San Francisco, 1971), pp. 86–116.
- ³³G. M. Whitesides, E. Ostuni, S. Takayama, X. Jiang, and D. E. Ingber, *Annu. Rev. Biomed. Eng.* **3**, 335 (2001).
- ³⁴K. Haubert, T. Drier, and D. Beebe, *Lab Chip* **6**, 1548 (2006).
- ³⁵J. Schindelin, I. Arganda-Carreras, E. Frise, V. Kaynig, M. Longair, T. Pietzsch, S. Preibisch, C. Rueden, S. Saalfeld, B. Schmid, J.-Y. Tinevez, D. J. White, V. Hartenstein, K. Eliceiri, P. Tomancak, and A. Cardona, *Nat. Methods* **9**, 676 (2012).
- ³⁶E. Meijering, O. Dzyubachyk, and I. Smal, *Method Enzymol.* **504**, 183 (2012).
- ³⁷S. T. Mortimer and D. Mortimer, *J. Androl.* **11**, 195 (1990).
- ³⁸S. Rode, J. Elgeti, and G. Gompper, *New J. Phys.* **21**, 013016 (2019).
- ³⁹G. Corkidi, B. Taboada, C. D. Wood, A. Guerrero, and A. Darszon, *Biochem. Biophys. Res. Commun.* **373**, 125 (2008).